

System-Level Error Propagation and Tail-Risk Amplification in Reference-Based Robotic Navigation

Ning Hu^{1*}, Maochen Li², Senhao Cao³

¹ Department of Mechanical, Aerospace and Biomedical Engineering, University of Tennessee, Knoxville, TN 37916, USA

² ZOEZEN ROBOT CO.LTD, Beijing, China

³ Northeastern University, Boston, MA 02115, USA

*Correspondence: nhu2@vols.utk.edu

Abstract— Image guided robotic navigation systems frequently rely on reference-based geometric perception pipelines, where accurate spatial mapping is established through multi-stage estimation processes. In biplanar X-ray-guided navigation, such pipelines are widely adopted due to their real-time capability and geometric interpretability. However, navigation reliability is often constrained by an overlooked system-level failure mechanism in which installation-induced structural perturbations introduced at the perception stage can be progressively amplified along the perception–reconstruction–execution chain and ultimately dominate execution-level error and tail-risk behavior. This paper investigates this mechanism from a system-level perspective and presents a unified error propagation modeling framework that explicitly characterizes how installation-induced structural perturbations propagate and couple with pixel-level observation noise through biplanar imaging, projection matrix estimation, triangulation, and coordinate mapping. By combining first order analytic uncertainty propagation with large-scale Monte Carlo simulations, we analyze dominant sensitivity channels and quantify worst-case error behavior beyond mean accuracy metrics. The results demonstrate that rotational installation error acts as a primary driver of system level error amplification, whereas translational misalignment of comparable magnitude plays a secondary role under typical biplanar geometries. Moreover, installation-induced structural perturbations fundamentally alter the system’s sensitivity to perception noise, leading to pronounced tail-risk amplification that cannot be captured by additive error models. Real biplanar X-ray bench-top experiments further confirm that the predicted error amplification trends persist under realistic imaging and feature extraction uncertainty. Beyond the specific context of biplanar X-ray navigation, the findings reveal a broader structural limitation of reference-based, multi-stage geometric perception pipelines in robotics. By explicitly modeling system-level error propagation and tail-risk behavior, this work formulates a systematic framework for reliability assessment, sensitivity analysis, and risk-aware design in safety-critical robotic navigation systems.

Keywords— *System-level error propagation, Tail-risk amplification, Reference-based navigation, Geometric perception pipelines, Multi-stage geometric estimation, Uncertainty propagation, Sensitivity analysis, Biplanar X-ray navigation, Safety-critical robotic systems*

I. INTRODUCTION

Robotic systems are increasingly deployed in safety-critical applications that require precise geometric reasoning under stringent reliability constraints, such as image-guided

intervention, surgical navigation, and reference-based robotic manipulation [1-3]. In these settings, even millimeter-level deviations may lead to irreversible consequences, motivating the widespread use of image-guided navigation systems that establish spatial mappings between perception and execution through geometric reference structures [4-5].

A representative class of such systems relies on reference-based, multi-stage geometric perception pipelines, in which spatial relationships are inferred through a sequence of estimation steps, including image formation, projection matrix estimation, geometric reconstruction, and coordinate mapping [6-9]. In biplanar X-ray-guided navigation, for example, multiple projection views are combined with a known 3D reference structure to reconstruct target positions and guide robotic execution. Due to their geometric interpretability and real-time capability, such pipelines are commonly assumed to be reliable once local calibration accuracy and image noise are adequately controlled.

This assumption underlies most navigation system designs, where reliability is typically evaluated using mean accuracy metrics and improvement efforts focus on reducing component-level uncertainties such as pixel noise, calibration error, or registration residuals[10-11]. However, empirical observations from real systems increasingly contradict this view. Even when local error metrics appear well controlled, execution-level deviations may still become large, anisotropic, and directionally biased, reflecting how errors propagate and interact across the entire perception–reconstruction–execution chain[12-13].

In particular, installation-induced structural perturbations—such as small misalignments of reference structures that are ubiquitous in practical systems—introduce biased geometric inputs that cannot be eliminated through calibration alone. How such structural perturbations propagate through nonlinear geometric estimation pipelines, and whether they can systematically dominate worst-case navigation behavior, remains insufficiently characterized.

From a system-level perspective, this paper investigates the following question: under what conditions do small structural perturbations in a geometric reference configuration become systematically amplified into large execution-level errors, even when local calibration accuracy is high? We argue that this phenomenon reflects an inherent limitation of reference-based, multi-stage geometric perception pipelines. Specifically,

installation-induced perturbations bias the 3D control point configuration used for projection matrix estimation and are subsequently amplified through nonlinear processes such as biplanar triangulation and coordinate mapping, leading to pronounced tail-risk behavior that is not captured by mean accuracy metrics.

To study this mechanism in a concrete and analytically tractable setting, we focus on biplanar X-ray-based 3D localization as a representative instance of reference-driven perception pipelines[6-8]. While often assumed to be robust once calibration and image noise are controlled, we show that even small installation misalignments—particularly rotational perturbations—can fundamentally alter system sensitivity and dominate navigation reliability through coupled amplification across estimation stages.

Motivated by this insight, we develop a unified system-level error propagation modeling framework that spans biplanar imaging, projection matrix estimation, 3D reconstruction, and coordinate mapping. Grounded in uncertainty propagation theory, the framework explicitly characterizes how installation-induced structural perturbations propagate and couple with pixel-level observation noise. The proposed analysis reveals that rotational installation error acts as a dominant sensitivity channel governing both localization accuracy and tail-risk behavior, whereas translational misalignment of comparable magnitude plays a secondary role under typical biplanar configurations.

The framework is validated through a combination of first-order analytic uncertainty propagation, large-scale Monte Carlo simulations, and real biplanar X-ray phantom experiments. These experiments are designed not as performance benchmarks, but as mechanism validation, establishing consistency between analytic prediction, statistical characterization, and real-system behavior.

Importantly, this work does not aim to introduce a new navigation algorithm or calibration procedure. Instead, it exposes a structural failure mechanism in reference-based geometric perception pipelines that persists even under high local accuracy. By explicitly modeling system-level error propagation and tail-risk behavior, this study provides a principled foundation for reliability assessment, sensitivity analysis, and risk-aware design in safety-critical robotic navigation systems.

The main contributions of this work are threefold. First, we identify and formalize a system-level error amplification mechanism in reference-based, multi-stage geometric perception pipelines. Second, we quantitatively characterize the coupled amplification between installation-induced structural perturbations and pixel-level perception noise, demonstrating that system-level error behavior is not a linear superposition of individual error sources. Third, we establish a unified perspective linking analytic prediction, statistical characterization, and real-system validation, clarifying the predictive scope and linearization limits of first-order uncertainty propagation models.

II. RELATED WORK

This section reviews prior work on biplanar X-ray-based navigation, geometric reconstruction, calibration, and error modeling, and clarifies why existing approaches, despite their technical maturity, remain insufficient to explain the system-level error amplification phenomena studied in this paper.

A. *Intraoperative Navigation and Biplanar X-ray-Based Localization*

Biplanar X-ray-based navigation systems have been widely adopted in orthopedic and neurosurgical procedures due to their intuitive imaging geometry, real-time feedback, and minimal invasiveness [1-5]. Such systems typically combine multi-view projection images with known reference structures or preoperative CT data to enable three-dimensional localization and surgical guidance.

Prior work has primarily focused on improving navigation accuracy through enhanced 2D–3D registration and reconstruction pipelines. For example, Yang et al. [14] proposed an improved biplanar reconstruction framework, while datasets such as Guide3D [15] facilitated standardized evaluation of biplanar X-ray-based 3D reconstruction methods. These efforts have significantly advanced reconstruction fidelity and benchmarking practice.

However, most existing approaches implicitly assume that reference structures and their installation are sufficiently reliable once calibration is completed. As a result, research has largely concentrated on reducing algorithmic or imaging noise, whereas the possibility that small installation-induced structural perturbations may propagate through the geometric estimation pipeline and dominate worst-case navigation behavior remains underexplored. This work addresses this gap by analyzing biplanar navigation reliability from a system-level error propagation perspective.

B. *Biplanar Geometry and 3D Reconstruction*

Biplanar 3D localization methods generally fall into two categories: geometry-driven approaches that estimate projection matrices from 3D–2D correspondences and perform triangulation-based reconstruction, and 2D–3D registration methods based on intensity or feature consistency.

The theoretical foundations of multi-view geometry, including pinhole imaging models, projection matrix estimation, and triangulation, are well established [6][7][8]. Previous studies have also examined the influence of view configuration and projection geometry on reconstruction quality under realistic fluoroscopic conditions[16]. Despite these advances, deviations in control point coordinates or pixel observations—such as those induced by installation error—are typically treated as independent measurement noise.

The structural nature of installation-induced perturbations, which bias the 3D reference configuration prior to projection matrix estimation and may be subsequently amplified through triangulation and coordinate mapping, has received limited attention. By explicitly modeling such perturbations and tracing their propagation through the biplanar geometric pipeline, the present work reframes reconstruction error analysis as a

navigation reliability problem with explicit tail-risk characterization.

C. Robot–Imaging Calibration and TCP / Hand–Eye Error Chains

In image-guided robotic navigation systems, mapping reconstructed targets from the imaging or reference frame to the robot tool center point (TCP) requires a sequence of extrinsic calibrations, including hand–eye calibration and TCP definition[9]. Numerous studies have investigated both marker-based and markerless calibration strategies to improve calibration accuracy and repeatability[17] [18][19].

While these works provide valuable insights into individual calibration components, they typically address each transformation in isolation. In practical navigation systems, however, calibration errors and installation-induced structural deviations accumulate across multiple stages and interact with upstream geometric estimation. How such coupled errors shape execution-level error boundaries and worst-case behavior remains insufficiently modeled. This work isolates the perception–geometry chain and provides a unified framework for incorporating calibration-related uncertainty into system-level error propagation analysis.

D. Error Modeling and Uncertainty Propagation in Medical Navigation

Error modeling and uncertainty propagation are central topics in medical navigation research. Classical analyses established that target point accuracy, rather than fitting accuracy at registration landmarks, should serve as the primary evaluation metric[10,20]. Subsequent studies further investigated the spatial properties of target registration error and the influence of imaging configuration on registration accuracy [21] [22].

Despite this extensive literature, most existing error modeling approaches focus on local propagation from registration or calibration error to target error, typically assuming linearized behavior and emphasizing mean or variance-based metrics. The error source emphasized in this paper—installation-induced structural perturbations in 3D control point inputs—has received comparatively little attention. Such perturbations enter the projection matrix estimation stage and may be nonlinearly amplified through biplanar triangulation and coordinate mapping, leading to coupled tail-risk behavior that is not captured by conventional local error models.

E. Summary

In summary, prior research has established strong foundations in biplanar reconstruction, 2D–3D registration, calibration, and uncertainty analysis. However, a unified framework that spans installation-induced structural perturbations, projection matrix estimation, triangulation, and coordinate mapping—and that explicitly characterizes error coupling and worst-case risk—remains lacking. The present work addresses this gap by proposing and validating a system-level error propagation model under typical biplanar geometric configurations, revealing the dominant role of rotational

installation error as a system-level structural perturbation and its coupled amplification with pixel-level noise.

III. METHODOLOGY

Fig. 1 provides an overview of the system-level error propagation pipeline examined in this work. The navigation system follows a representative reference-based geometric perception workflow, in which a known three-dimensional reference structure is observed by a biplanar C-arm X-ray imaging system, reconstructed through multi-stage geometric estimation, and mapped to the robot tool center point (TCP) for execution. While such pipelines are commonly assumed to be reliable once local calibration accuracy and imaging noise are sufficiently controlled, Fig. 1 highlights how installation-induced structural perturbations introduce biased geometric inputs at an early stage and are subsequently amplified through successive estimation and transformation steps.

Specifically, small but biased rotational and translational misalignments in the reference configuration alter the effective 3D control point geometry used for projection matrix estimation. These perturbations interact with pixel-level observation noise, degrade the conditioning of geometric estimation, and propagate nonlinearly through biplanar triangulation and coordinate mapping. As a result, reconstruction uncertainty becomes anisotropic and heavy-tailed, and subsequent mapping to the robot/TCP frame further compounds—rather than attenuates—these errors. This section formalizes this mechanism and establishes a unified framework for analyzing system-level error amplification. Detailed derivations are provided in the Supplementary Material.

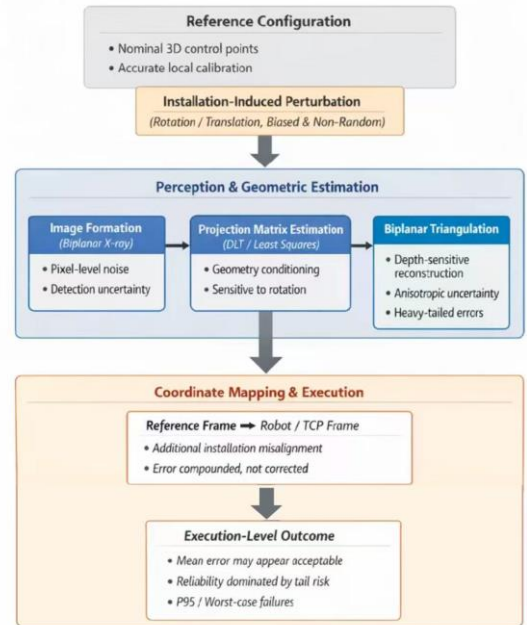


Fig 1. Overview of system-level error propagation in reference-based geometric perception pipelines. Installation-induced structural perturbations introduce biased geometric inputs at the perception stage, which are nonlinearly amplified through projection matrix estimation, biplanar triangulation, and coordinate mapping. This amplification fundamentally alters system sensitivity to perception noise and leads to heavy-tailed execution-level error distributions, where tail risk rather than mean accuracy dominates navigation reliability.

A. Imaging and Localization Overview

In biplanar X-ray-guided robotic navigation, a known three-dimensional reference structure rigidly attached to the robot is observed from two distinct imaging views. Two-dimensional projections of reference features are associated with their nominal three-dimensional coordinates to estimate view-dependent projection matrices, and target points are reconstructed via biplanar triangulation. The reconstructed target position is then mapped through a sequence of coordinate transformations to the robot tool center point (TCP) frame for execution. This reference-based, multi-stage geometric pipeline is widely adopted due to its real-time capability and geometric interpretability. In this work, the formulation is treated as a baseline, and emphasis is placed on how deviations in the assumed reference geometry propagate through this pipeline and affect execution-level reliability.

B. Structural Error Propagation Mechanism

Installation-induced structural perturbations are modeled as small but systematic structural deviations in the assumed geometry of the reference structure prior to geometric estimation. These perturbations enter the navigation pipeline before projection matrix estimation and therefore bias the geometric model itself, rather than appearing as additive measurement noise. As a result, their influence propagates through all subsequent stages of the perception–reconstruction–execution chain.

Because projection matrix estimation and biplanar triangulation are nonlinear and geometry-dependent, biased reference configurations fundamentally alter system sensitivity to pixel-level observation noise. In particular, rotational misalignments globally distort the spatial arrangement of control points and dominate error amplification, whereas translational deviations of comparable magnitude introduce only secondary effects under typical biplanar configurations. Subsequent coordinate mapping to the robot tool center point (TCP) frame further compounds these errors rather than correcting them, leading to execution-level deviations characterized by strong anisotropy and heavy-tailed behavior.

C. Uncertainty and Tail-Risk Analysis

System-level uncertainty is analyzed using a combination of first-order analytic propagation and Monte Carlo simulation. Analytic propagation captures dominant sensitivity directions and relative error scaling, providing interpretable insight into how structural perturbations reshape the system’s sensitivity landscape. Monte Carlo analysis complements this by capturing nonlinear effects and non-Gaussian error distributions arising from coupled geometric estimation. Rather than emphasizing mean localization accuracy, navigation reliability is evaluated using tail-risk metrics, such as high-percentile execution error, which better reflect worst-case failure modes in safety-critical robotic navigation. Together, these analyses reveal how installation-induced structural perturbations couple with perception noise to dominate execution-level reliability and failure behavior.

IV. EXPERIMENTS AND ANALYSIS

A. Experimental Objectives and Validation Logic

The experiments are designed to validate the system-level error propagation mechanism induced by installation-induced structural perturbations. Specifically, we aim to answer three questions: (1) where structural errors enter the perception–reconstruction–execution pipeline and how they are amplified; (2) whether installation errors couple with perception noise in a non-additive manner; and (3) whether the proposed model captures dominant sensitivity channels and tail-risk behavior. To this end, two simulation studies are conducted to isolate the primary and coupled effects of installation error, followed by a minimal physical phantom experiment to verify that the observed mechanisms persist under real imaging conditions.

B. Simulation Study I: Primary Effect of Installation Error

We first examine whether installation-induced structural perturbations constitute the dominant driver of system-level error amplification. Pixel-level noise is fixed at a negligible level, while rotational and translational installation errors are independently varied to isolate their respective effects on localization and execution accuracy.

As shown in Fig. 2, both the 3D localization error and the TCP execution error increase monotonically with rotational installation misalignment. Increasing the rotation error from 0° to 2° leads to a substantial growth in both mean error and tail-risk metrics, indicating pronounced amplification of execution-level deviation. In this experiment, the TCP transformation is assumed to be an ideal rigid-body mapping without additional execution uncertainty. Consequently, execution error closely matches localization error magnitude, demonstrating that structural perturbations introduced at the perception and reconstruction stages alone are sufficient to determine the upper bound and tail-risk behavior of navigation accuracy.

In contrast, translational installation error produces only marginal variations in both localization and execution error over the tested range, as illustrated in Fig. 3. This sharp asymmetry confirms that, under the tested biplanar geometry and target scale, rotational misalignment constitutes the dominant structural error source, whereas translational deviations of comparable magnitude act primarily as secondary perturbations. This distinction highlights the fundamentally different roles of rotational and translational installation errors in shaping system-level sensitivity and reliability. Quantitative results for simulation I configurations, including full error statistics and tail-risk metrics, are summarized in the Supplementary Material.

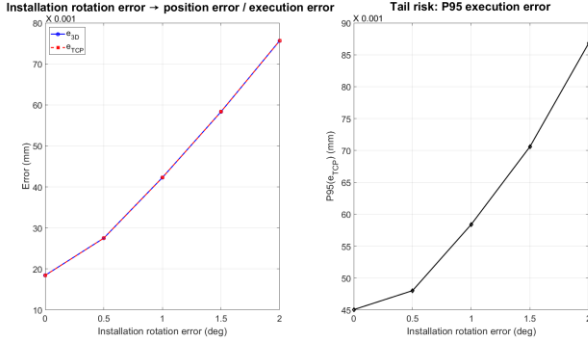


Fig.2. Effect of installation rotation error. Left: localization and execution errors increase approximately linearly with rotation misalignment. Right: tail risk (P95) of execution error grows significantly with installation error.



Fig.3. Effect of installation translation error. Translation misalignment introduces relatively minor perturbations compared to rotational errors under the tested geometry.

C. Simulation Study II: Coupled Amplification of Installation Error and Pixel Noise

In practical robotic navigation systems, installation-induced structural perturbations and pixel-level perception noise coexist. To examine their interaction, we conduct a coupled simulation study in which installation error levels and pixel noise magnitude are jointly varied, and execution-level tail-risk metrics are evaluated.

As shown in Fig. 4, pixel noise and installation-induced structural perturbations exhibit a pronounced non-additive coupling effect. In the absence of installation error, increasing pixel noise leads to a relatively bounded growth in execution error. Once installation-induced structural perturbations are introduced, however, the same level of pixel noise produces a substantially larger increase in tail risk. This sharp change in sensitivity indicates that installation error fundamentally reshapes the system's response to perception noise.

These results demonstrate that system-level error cannot be explained as a simple superposition of independent noise sources. Instead, installation-induced structural perturbations alter the geometric conditioning of the estimation pipeline, transforming otherwise tolerable perception noise into a navigation-level risk factor through coupled amplification.

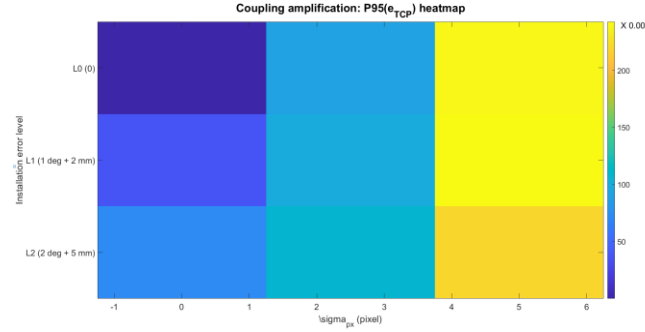


Fig.4. Coupled amplification of pixel noise and installation error. Tail risk (P95) of execution error increases sharply with pixel noise under different installation error levels.

D. Physical Phantom Experiment

To validate the simulation findings at the execution level, a minimal biplanar X-ray phantom experiment is conducted under controlled installation conditions. The reference structure is installed with increasing levels of misalignment, and biplanar images are repeatedly acquired to estimate localization error and tail-risk metrics.

Experimental results exhibit a clear monotonic increase in error magnitude and tail risk with increasing installation perturbation, consistent with simulation predictions in both trend and relative magnitude. These results confirm that the identified system-level error amplification mechanism persists under realistic imaging and detection uncertainty. Quantitative results for simulation II configurations, including full error statistics and tail-risk metrics, are summarized in the Supplementary Material.

To further assess the predictive scope and limitations of first-order analytic uncertainty propagation, we compare analytic predictions with Monte Carlo statistics under a representative operating condition. Detailed results and discussion are provided in the Supplementary Material.

E. Summary

Across simulation and real-system validation, the results establish a coherent evidence chain demonstrating that installation-induced structural perturbations act as a dominant driver of system-level error amplification. The observed coupled interaction between structural perturbations and perception noise further highlights the limitation of local accuracy metrics and motivates a shift from local accuracy optimization toward end-to-end, system-level reliability analysis in reference-based geometric navigation systems.

V. REAL-SYSTEM VALIDATION

To examine whether the identified system-level error amplification mechanism persists under real imaging conditions, we conduct a biplanar X-ray bench-top experiment. This experiment is not intended as a clinical evaluation, but as a mechanism validation to assess whether the error propagation behaviors revealed by simulation remain observable in a real navigation pipeline subject to imaging noise and feature extraction uncertainty.

As shown in Fig. 5, a C-arm X-ray system acquires anteroposterior (AP) and lateral (LAT) views of a localization reference structure mounted to a rigid phantom. Due to practical engineering constraints, rotational and translational installation errors cannot be independently controlled. Instead, a level-based installation strategy is adopted, defining three representative conditions: ideal installation (L0), moderate misalignment (L1), and larger misalignment (L2). Each condition is repeated with full disassembly and reinstallation to ensure that observed variability reflects installation-induced effects.

Across installation levels, both localization error and tail-risk metrics exhibit a clear monotonic increase, consistent with simulation predictions in trend and relative magnitude. Importantly, beyond quantitative metrics, the execution-level outcomes shown in Fig. 6 reveal visually apparent and directionally consistent degradation from L0 to L2, despite identical target definitions and nominal perception accuracy. This behavior indicates a structurally biased mapping rather than noise-induced fluctuation.

These real-system results provide direct qualitative and quantitative evidence that small installation-induced structural perturbations can be systematically amplified through the perception–reconstruction–execution chain. The observed trends closely mirror those identified in simulation, confirming that system-level error amplification and tail-risk-dominated behavior persist under realistic imaging conditions. Quantitative localization and reprojection error statistics for all installation conditions are summarized in the Supplementary Material.

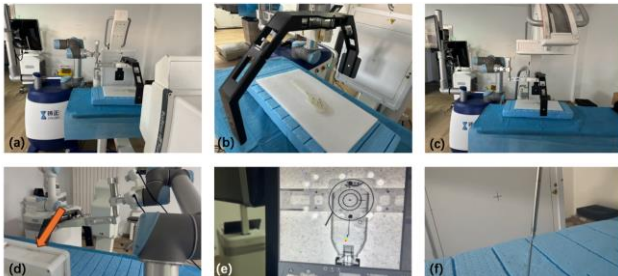


Fig.5 Real-system biplanar X-ray navigation setup and experimental configuration for system-level error propagation analysis. (a–c) Biplanar X-ray bench-top experimental setup under different installation states, illustrating the physical configuration used for real-system validation. (d) Geometric workflow of the biplanar X-ray-guided navigation pipeline, including reference-based projection matrix estimation, biplanar triangulation, and coordinate mapping to the robot execution frame. (e) Representative anteroposterior (AP) and lateral (LAT) X-ray views used for geometric localization. (f) Illustration of the execution task and positioning error definition following target insertion. Together, these components define the perception–reconstruction–execution chain through which installation-induced structural perturbations enter and propagate in the real system.

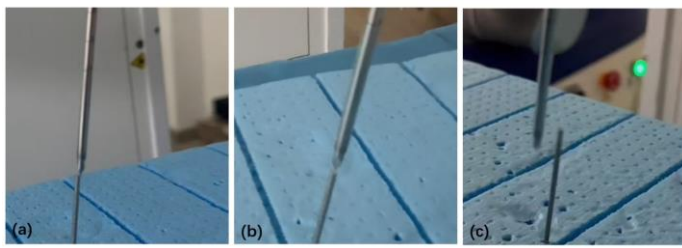


Fig. 6. Execution-level manifestation of system-level error amplification under increasing installation-induced perturbations. (a–c) Final execution

outcomes under three installation conditions: ideal installation (L0), moderate misalignment (L1), and larger misalignment (L2), corresponding to increasing levels of installation-induced structural perturbation. Despite identical target definitions and nominal perception accuracy, the execution result exhibits a visually apparent and monotonic degradation from L0 to L2. The observed deviation is directionally consistent across trials, indicating a structurally biased mapping rather than noise-induced fluctuation. These execution-level outcomes provide qualitative but direct evidence that small structural perturbations introduced at the perception stage can be systematically amplified through the perception–reconstruction–execution chain, leading to tail-risk-dominated failures.

VI. DISCUSSION

This work investigates a system-level failure mechanism in reference-based geometric perception pipelines, demonstrating that installation-induced structural perturbations can be systematically amplified through multi-stage estimation and ultimately dominate execution-level reliability. Rather than treating errors as independent noise sources confined to individual modules, our results show that error propagation is an inherent structural property of the perception–reconstruction–execution chain, arising from the interaction between biased geometric inputs and nonlinear geometric estimation. A key insight is the pronounced asymmetry between rotational and translational installation perturbations. Rotational misalignment globally distorts the spatial configuration of reference control points, degrading the conditioning of projection matrix estimation and biplanar triangulation in a manner that accumulates across stages. In contrast, translational deviations of comparable magnitude introduce only localized disturbances and remain secondary under typical biplanar geometries. This distinction highlights that not all installation errors are equally consequential and has direct implications for tolerance allocation and calibration prioritization in reference-based navigation systems. Beyond the primary effect of installation error, the results reveal that system-level error behavior cannot be explained as a linear superposition of structural perturbations and perception noise. Once installation-induced perturbations are present, the system’s sensitivity to pixel-level uncertainty is fundamentally reshaped, transforming otherwise tolerable noise into a navigation-level risk factor through coupled amplification. This behavior cannot be mitigated through local improvements alone, such as incremental calibration refinement or enhanced feature detection, and instead reflects a shift in dominant sensitivity channels at the system level. Importantly, the real-system biplanar X-ray experiment confirms that the identified amplification mechanism persists under realistic imaging conditions. The execution-level outcomes exhibit monotonic and directionally consistent degradation with increasing installation perturbation, indicating structurally biased mapping rather than noise-induced fluctuation. These observations demonstrate that the predicted tail-risk behavior is not merely a statistical artifact but manifests as qualitatively distinct execution failures in a real navigation pipeline. The implications of these findings extend beyond the specific context of biplanar X-ray-guided navigation. Although this study adopts biplanar X-ray imaging as a representative instance, the identified amplification mechanism reflects a general structural limitation of reference-based, multi-stage geometric perception pipelines. Small structural perturbations introduced early in the estimation chain can be systematically amplified into execution-level failures, underscoring the need to move beyond mean-accuracy

based evaluation toward risk-aware, system-level reliability analysis. While execution-side uncertainties such as hand–eye calibration error, tool center point definition error, and manipulator compliance are not explicitly modeled here, they can be naturally incorporated into the proposed framework by treating execution-stage transformations as additional random variables. Importantly, the presence of such uncertainties would compound, rather than eliminate, the system-level amplification mechanism identified in this work. Overall, this study provides a unified system-level perspective on error propagation and tail-risk emergence in geometric perception pipelines. By integrating analytic modeling, simulation, and real-system execution-level validation, the results motivate a shift from component-wise accuracy optimization toward risk-aware, system-level design and evaluation in safety-critical robotic navigation systems.

VII. CONCLUSION

This paper examined a system-level error propagation mechanism in reference-based geometric perception pipelines, with a particular focus on installation-induced structural perturbations. Rather than treating uncertainty as independent noise confined to individual modules, we showed that installation error propagates along multi-stage geometric estimation chains—from projection matrix estimation and biplanar triangulation to coordinate mapping—and is systematically amplified through nonlinear coupling with perception noise, giving rise to pronounced tail-risk behavior that ultimately dominates execution-level reliability.

Through three complementary simulation studies, we demonstrated that rotational installation error constitutes the primary driver of navigation error amplification under typical biplanar geometries, whereas translational misalignment of comparable magnitude plays a secondary role. First-order analytic uncertainty propagation captures dominant error directions and relative magnitude relationships, while Monte Carlo analysis remains essential for conservative estimation of worst-case risk in strongly nonlinear regimes. Together, these results clarify both the dominant sensitivity channels governing system-level behavior and the predictive limits of linearized analytic models.

Importantly, a real-system biplanar X-ray bench-top experiment confirmed that the identified error amplification mechanism persists under realistic imaging and feature extraction uncertainty. The monotonic growth in both mean localization error and P95 tail-risk metrics across installation levels, together with execution-level outcomes exhibiting visually apparent and directionally consistent degradation, demonstrates that the predicted tail-risk behavior is not a simulation artifact but manifests as qualitative execution-level failure in a real navigation pipeline.

Beyond the specific context of biplanar X-ray–guided navigation, these findings reveal a broader structural limitation of reference-based, multi-stage geometric perception pipelines in robotics: small structural perturbations introduced early in the estimation chain can be systematically amplified into execution-level failures that are not captured by mean accuracy metrics alone. By explicitly modeling system-level error propagation and tail-risk behavior, this work provides a unified and

extensible framework for sensitivity analysis, reliability assessment, and risk-aware design in safety-critical robotic navigation systems.

Future work will extend this framework to incorporate execution-side uncertainties, such as hand–eye calibration error and manipulator compliance, and to explore risk-aware calibration, planning, and navigation strategies informed by system-level error propagation.

REFERENCES

- [1] S. LAVALLEE, ‘Computer-assisted spinal surgery using anatomy-based registration’, *Computer Integrated Surgery and Clinical Application*, 1995.
- [2] K. Cleary and T. M. Peters, ‘Image-guided interventions: technology review and clinical applications’, *Annu. Rev. Biomed. Eng.*, vol. 12, no. 1, pp. 119–142, 2010.
- [3] T. M. Peters, ‘Image-guided surgery: from X-rays to virtual reality’, *Comput. Methods Biomed. Engin.*, vol. 4, no. 1, pp. 27–57, 2001.
- [4] ‘Image-guided navigation in spine surgery: from historical developments to future perspectives’, *J. Clin. Med.*, vol. 13, no. 7, 2024.
- [5] S. Rajasekaran, V. R. Tubaki, and A. P. Shetty, ‘Results of direct repair of type 2 hangman fracture using Iso-C3D navigation: 20 cases’, *Clin. Spine Surg.*, vol. 25, no. 5, pp. 134–139, 2012.
- [6] R. Hartley and A. Zisserman, ‘Multiple view geometry in computer vision’, 2003.
- [7] O. Faugeras, *Three-dimensional computer vision: a geometric viewpoint*. MIT press, 1993.
- [8] A. A. YI, ‘Direct linear transformation from comparator coordinates into object space coordinates’, in *Proceedings of the ASP/UI Symposium on Close-Range Photogrammetry*, Urbana, IL: American Society of Photogrammetry, 1971.
- [9] R. H. Taylor, A. Menciassi, G. Fichtinger, P. Fiorini, and P. Dario, ‘Medical robotics and computer-integrated surgery’, in *Springer handbook of robotics*, Cham: Springer International Publishing, 2016, pp. 1657–1684.
- [10] J. M. Fitzpatrick and J. B. West, ‘The distribution of target registration error in rigid-body point-based registration’, *IEEE Trans. Med. Imaging*, vol. 20, no. 9, pp. 917–927, 2002.
- [11] C. R. Maurer, ‘A review of medical image registration’, *Interactive imageguided neurosurgery*, vol. 66, no. 2, p. 17, 1993.
- [12] A. Danilchenko and J. M. Fitzpatrick, ‘General approach to first-order error prediction in rigid point registration’, *IEEE Trans. Med. Imaging*, vol. 30, no. 3, pp. 679–693, 2010.
- [13] J. Liang, Y. Ye, D. Wu, B. Ren, and Z. Song, ‘Automated Precise 3D Measurement of Featureless Surfaces Assisted by Laser Grids Projection’, *IEEE Trans. Instrum. Meas.*, 2025.

- [14] D. Yang, H. Shi, B. Zeng, and X. Chen, ‘2D/3D registration based on biplanar X-ray and CT images for surgical navigation’, *Comput. Methods Programs Biomed.*, vol. 257, p. 108444, 2024.
- [15] T. Jianu *et al.*, ‘Guide3D: A Bi-planar X-ray Dataset for Guidewire Segmentation and 3D Reconstruction’, in *Proceedings of the Asian Conference on Computer Vision*, 2024, pp. 1549–1565.
- [16] S. Jecklin *et al.*, ‘Domain adaptation strategies for 3D reconstruction of the lumbar spine using real fluoroscopy data’, *Med. Image Anal.*, vol. 98, p. 103322, 2024.
- [17] P. Markelj, D. Tomaževič, B. Likar, and F. Pernuš, ‘A review of 3D/2D registration methods for image-guided interventions’, *Med. Image Anal.*, vol. 16, no. 3, pp. 642–661, 2012.
- [18] Y. Liu, J. Zhang, Z. She, A. Kheradmand, and M. Armand, ‘Gbec: Geometry-based hand-eye calibration’, in *2024 IEEE International Conference on Robotics and Automation (ICRA)*, IEEE, 2024, pp. 16698–16705.
- [19] L. Zhang, C. Li, Y. Fan, X. Zhang, and J. Zhao, ‘Physician-friendly tool center point calibration method for robot-assisted puncture surgery’, *Sensors*, vol. 21, no. 2, p. 366, 2021.
- [20] A. Seginer, ‘Rigid-body point-based registration: The distribution of the target registration error when the fiducial registration errors are given’, *Med. Image Anal.*, vol. 15, no. 4, pp. 397–413, 2011.
- [21] A. Uneri *et al.*, ‘3D–2D registration for surgical guidance: effect of projection view angles on registration accuracy’, *Phys. Med. Biol.*, vol. 59, no. 2, p. 271, 2013.
- [22] P. Jackson, R. Simon, and C. Linte, ‘(February). Effect of uncertainty on target registration error in image-guided renal interventions: from simulation to in-vitro assessment’, in *Medical Imaging 2021: Image-Guided Procedures, Robotic Interventions, and Modeling*, vol. 11598, SPIE, 2021, pp. 117–124.

Supplementary

I. METHODOLOGY

A. Imaging and Localization Overview

In medical image-guided navigation, C-arm X-ray imaging can be abstracted as a pinhole camera system. The pinhole camera model is one of the most widely used geometric models in computer vision, describing the mapping from three-dimensional space to the two-dimensional image plane through linear projection. Its core lies in estimating the intrinsic and extrinsic parameters of the imaging system.

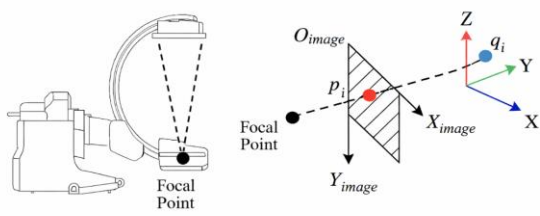


Fig. S1 Overview of Camera Imaging Model and Localization

As illustrated in Fig. S1, the X-ray pinhole camera model maps a 3D feature point expressed in the object coordinate system to the X-ray image coordinate system via a projective transformation. The mapping equation is given by:

$$\begin{aligned} \mathbf{p} &= \mathbf{A}\mathbf{q} \\ \mathbf{p} &= s[u \ v \ 1]^\top, \\ \mathbf{A} &= \begin{bmatrix} A_1 & A_2 & A_3 & A_4 \\ A_5 & A_6 & A_7 & A_8 \\ A_9 & A_{10} & A_{11} & A_{12} \end{bmatrix}, \\ \mathbf{q} &= [x \ y \ z \ 1]^\top \end{aligned} \quad (1)$$

Where \mathbf{p} denotes the homogeneous 2D coordinates of a feature point in the X-ray image coordinate system, \mathbf{q} denotes the homogeneous 3D coordinates of the corresponding feature point in the object coordinate system, s is a scale factor, $[u \ v \ 1]^\top$ represents the image coordinates, \mathbf{A} is the transformation (projection) matrix, and $[x \ y \ z \ 1]^\top$ denotes the 3D coordinates in the target coordinate system. The transformation matrix \mathbf{A} contains 12 unknown parameters. Substituting the coordinates into the mapping equation yields:

Here \mathbf{x}_i denotes the homogeneous 2D image coordinates of the feature point in the X-ray image, $\tilde{\mathbf{X}}_i$ represents the homogeneous 3D coordinates of the corresponding feature point

in the object coordinate system, λ is a scale factor, and \mathbf{P} is the projection matrix. The projection matrix \mathbf{P} contains 12 unknown parameters and encapsulates both intrinsic and extrinsic imaging geometry.

$$\begin{aligned} (A_1 - A_9 u)x + (A_2 - A_{10} u)y + (A_3 - A_{11} u)z + (A_4 - A_{12} u) &= 0 \\ (A_5 - A_9 v)x + (A_6 - A_{10} v)y + (A_7 - A_{11} v)z + (A_8 - A_{12} v) &= 0 \end{aligned} \quad (2)$$

That is, $G_u(\tilde{\mathbf{A}}, \mathbf{p}, \mathbf{q}) = 0$ and $G_v(\tilde{\mathbf{A}}, \mathbf{p}, \mathbf{q}) = 0$. Using n point correspondences, a system of $2n$ nonlinear equations can be constructed, i.e.,

$$G(\tilde{\mathbf{A}}, \mathbf{a}) = 0 \quad (3)$$

Where $\tilde{\mathbf{A}} = [A_1, A_2, \dots, A_{12}]^\top$, $\mathbf{a} = [\mathbf{a}_1, \mathbf{a}_2, \dots, \mathbf{a}_n]^\top$, $\mathbf{a} = [x, y, z, u, v]$, (3) can be solved using a least-squares formulation.

To achieve three-dimensional localization of a target point, the system requires X-ray images acquired from at least two distinct viewing angles. In practice, a biplanar configuration is typically adopted, consisting of anteroposterior (AP) and lateral (LAT) views. Under ideal, noise-free conditions, two projection matrices can be estimated by solving Eq. (3) for each view. Given a corresponding point observed in both images, its three-dimensional position can then be reconstructed through the intersection of the associated projection rays.

$$\mathbf{p}_1 = \mathbf{A} \cdot \mathbf{q}_{\text{aim}}, \quad \mathbf{p}_2 = \mathbf{B} \cdot \mathbf{q}_{\text{aim}} \quad (4)$$

$$s \begin{bmatrix} u_1 \\ v_1 \\ 1 \end{bmatrix} = \begin{bmatrix} A_{1,:} \\ A_{5,:} \\ A_{9,:} \end{bmatrix} \begin{bmatrix} x \\ y \\ z \end{bmatrix} \quad s \begin{bmatrix} u_2 \\ v_2 \\ 1 \end{bmatrix} = \begin{bmatrix} B_{1,:} \\ B_{5,:} \\ B_{9,:} \end{bmatrix} \begin{bmatrix} x \\ y \\ z \end{bmatrix} \quad (5)$$

$$(u_1 A_{9,:} - A_{1,:}) \begin{bmatrix} x \\ y \\ z \\ 1 \end{bmatrix} = 0 \quad (v_1 A_{9,:} - A_{5,:}) \begin{bmatrix} x \\ y \\ z \\ 1 \end{bmatrix} = 0 \quad (6)$$

$$(u_2 B_{9,:} - B_{1,:}) \begin{bmatrix} x \\ y \\ z \\ 1 \end{bmatrix} = 0 \quad (v_2 B_{9,:} - B_{5,:}) \begin{bmatrix} x \\ y \\ z \\ 1 \end{bmatrix} = 0 \quad (7)$$

The matrix \mathbf{N} is decomposed using singular value decomposition (SVD), $\mathbf{q}_{\text{aim}} = \text{SVD}(\mathbf{N})$, $\mathbf{N} = \mathbf{U} \mathbf{\Sigma} \mathbf{V}^\top$. The solution vector \mathbf{q}_{aim} is given by the right singular vector associated with the smallest singular value, i.e., the last column of \mathbf{V} . After normalization, \mathbf{q}_{aim} represents the reconstructed three-dimensional coordinates of the target point.

B. Structural Error Propagation Mechanism

Error Analysis

In practical image-guided surgical applications, various sources of uncertainty are inevitably introduced throughout the system, including measurement noise, numerical estimation error, and coordinate transformation inaccuracies. These errors do not exist in isolation within individual modules. Instead, they propagate and accumulate along the entire localization pipeline—spanning perception, geometric reconstruction, and coordinate mapping—and are progressively amplified through multi-stage geometric estimation. As a result, such system-level error propagation can substantially degrade three-dimensional target localization accuracy and ultimately compromise the execution accuracy of the robotic manipulator.

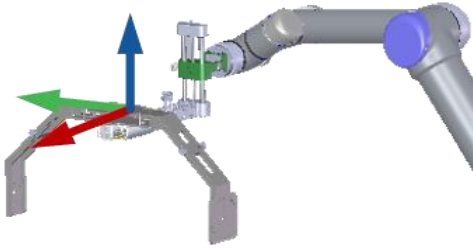


Fig.S2 Reference-based geometric perception pipeline in biplanar X-ray-guided robotic navigation. The C-arm X-ray imaging system acquires images of a localization reference structure rigidly attached to the robotic end effector. The reference structure consists of a set of fiducial points with known three-dimensional geometry. By detecting the two-dimensional pixel coordinates of these fiducials in the X-ray images and associating them with their pre-calibrated three-dimensional coordinates expressed in the connection.

As illustrated in Fig. S2, the C-arm X-ray imaging system acquires images of a localization reference structure rigidly attached to the end effector of the robotic manipulator. The reference structure contains a set of fiducial points with well-defined geometric features. By detecting the two-dimensional pixel coordinates of these fiducials in the X-ray images and associating them with their pre-calibrated three-dimensional coordinates expressed in the connector component coordinate frame, the system can estimate the transformation matrix from the connector component frame to the C-arm X-ray world coordinate frame by solving Eq. (3).

Under ideal, error-free conditions, this transformation matrix is denoted as $\mathbf{p} = \mathbf{A}_{\text{true}} \cdot \mathbf{q}_{\text{true}}$. However, in practical systems, installation-induced structural perturbations between the connector component and the localization reference structure introduce systematic errors into the input three-dimensional coordinates. As a result, the estimated transformation deviates from the ideal case and is instead represented as a perturbed transformation $\mathbf{q}_{\text{actual}} = \mathbf{T}_{\text{err1}} \mathbf{q}_{\text{true}}$.

Under this condition, Eq. (1) can be rewritten as:

$$\mathbf{p} = \mathbf{A}_{\text{actual}} \cdot \mathbf{T}_{\text{err1}} \cdot \mathbf{q}_{\text{true}} \quad (8)$$

It follows directly that the estimated transformation matrix becomes $\mathbf{A}_{\text{actual}} = \mathbf{A}_{\text{true}} \mathbf{T}_{\text{err1}}^{-1}$.

Under this condition, Eq. (4) can be rewritten as

$$\mathbf{p}_1 = \mathbf{A}_{\text{true}} \mathbf{T}_{\text{err1}}^{-1} \mathbf{q}_{\text{aim}}, \quad \mathbf{p}_2 = \mathbf{B}_{\text{true}} \mathbf{T}_{\text{err1}}^{-1} \mathbf{q}_{\text{aim}}.$$

$$\mathbf{p}_1 = \mathbf{A} \cdot \mathbf{q}_{\text{aim}}, \quad \mathbf{p}_2 = \mathbf{B} \cdot \mathbf{q}_{\text{aim}},$$

Compared with $\mathbf{p}_1 = \mathbf{A} \cdot \mathbf{q}_{\text{aim}}$, we can obtain that the perturbation in $\mathbf{T}_{\text{err1}}^{-1}$ directly affects the estimation of \mathbf{q}_{aim} . As a consequence, the resulting three-dimensional target position is obtained as $\mathbf{q}_{L1} = \mathbf{T}_{\text{err1}}^{-1} \mathbf{q}_{\text{aim}}$.

Since the estimated position \mathbf{q}_{L1} is expressed in the connector component coordinate frame, execution of the robotic motion requires transforming this position into the robot tool center point (TCP) coordinate frame.

$$\mathbf{q}_{\text{tcp}} = \mathbf{T}_{\text{tcp}}^{L2} \cdot \mathbf{T}_{L2}^{L1} \cdot \mathbf{q}_{L1} \quad (9)$$

In practice, installation-induced structural perturbations exist not only between the connector component and the localization reference structure, but also between the connector component and the robotic end effector. Consequently, the actual target position expressed in the TCP coordinate frame can be written as

$$\mathbf{q}_{\text{tcp}} = \mathbf{T}_{\text{tcp}}^{L2} \cdot \mathbf{T}_{L2}^{L1} \cdot \mathbf{T}_{\text{err2}} \cdot \mathbf{q}_{L1} \quad (10)$$

Under rigid-body kinematics, the installation-induced error \mathbf{T}_{err2} can be decomposed into a rotational perturbation about the x -, y -, and z -axes and a translational offset.

$$T_{rx} = \begin{bmatrix} 1 & 0 & 0 & 0 \\ 0 & \cos \alpha & -\sin \alpha & 0 \\ 0 & \sin \alpha & \cos \alpha & 0 \\ 0 & 0 & 0 & 1 \end{bmatrix}$$

$$T_{ry} = \begin{bmatrix} \cos \beta & 0 & \sin \beta & 0 \\ 0 & 1 & 0 & 0 \\ -\sin \beta & 0 & \cos \beta & 0 \\ 0 & 0 & 0 & 1 \end{bmatrix} \quad (11)$$

$$T_{rz} = \begin{bmatrix} \cos \gamma & -\sin \gamma & 0 & 0 \\ \sin \gamma & \cos \gamma & 0 & 0 \\ 0 & 0 & 1 & 0 \\ 0 & 0 & 0 & 1 \end{bmatrix}$$

$$T_t = \begin{bmatrix} 1 & 0 & 0 & \Delta x \\ 0 & 1 & 0 & \Delta y \\ 0 & 0 & 1 & \Delta z \\ 0 & 0 & 0 & 1 \end{bmatrix} \quad (12)$$

Since the rotation angles are typically small, a first-order small-angle approximation can be applied. Specifically, the cosine terms in the transformation matrix are approximated as unity, while the sine terms are approximated by the corresponding rotation angles. By neglecting higher-order terms, the perturbed transformation can be expressed as:

$$\mathbf{T}_{\text{err2}} = T_t * T_{rx} * T_{ry} * T_{rz} = T = \begin{bmatrix} 1 & -\gamma & \beta & \Delta x \\ \gamma & 1 & -\alpha & \Delta y \\ -\beta & \alpha & 1 & \Delta z \\ 0 & 0 & 0 & 1 \end{bmatrix} \quad (13)$$

Under this approximation, we obtain:

$$\mathbf{q}_{\text{tcp}} = \mathbf{T}_{\text{tcp}}^{L2} \cdot \mathbf{T}_{L2}^{L1} \cdot \begin{bmatrix} 1 & -\gamma & \beta & \Delta x \\ \gamma & 1 & -\alpha & \Delta y \\ -\beta & \alpha & 1 & \Delta z \\ 0 & 0 & 0 & 1 \end{bmatrix} \cdot \mathbf{T}_{\text{err1}}^{-1} \mathbf{q}_{\text{aim}} \quad (14)$$

It follows that both \mathbf{T}_{err1} and \mathbf{T}_{err2} directly influence the final localization of the target point.

C. Uncertainty and Tail-Risk Analysis

For Eq. (3), the three-dimensional coordinates of the control points \mathbf{q} and the corresponding two-dimensional image observations \mathbf{p} are modeled as mutually independent random variables following zero-mean Gaussian distributions.

Let $\Sigma_{\mathbf{A}}$ denote the covariance matrix of the output \mathbf{A} , and let $\Sigma_{\mathbf{a}}$ denote the covariance matrix of the input \mathbf{a} . According to the principle of uncertainty propagation, the following relationship holds:

$$\mathbf{J}_{\mathbf{A}} \Sigma_{\mathbf{A}} \mathbf{J}_{\mathbf{A}}^T = \mathbf{J}_{\mathbf{a}} \Sigma_{\mathbf{a}} \mathbf{J}_{\mathbf{a}}^T \quad (15)$$

Where $\Sigma_{\mathbf{a}} = \text{diag}\{\Sigma_{a_1}, \dots, \Sigma_{a_n}\}$,

$$\Sigma_{a_i} = \text{diag}\{u^2(x_i), u^2(y_i), u^2(z_i), u^2(u_i), u^2(v_i)\},$$

Here, $\mathbf{J}_{\mathbf{a}}$ denotes the Jacobian matrix of the function G with respect to the input vector \mathbf{a} , which consists of the three-dimensional control point coordinates x, y, z and the corresponding two-dimensional image observations u, v .

$\mathbf{J}_{\mathbf{a}} = \text{diag}\{\mathbf{J}_{a_1}, \dots, \mathbf{J}_{a_n}\}$, where \mathbf{J}_{a_i}

$$\mathbf{J}_{a_i} = \begin{bmatrix} \frac{\partial G_u(\mathbf{A}, p_i, q_i)}{\partial x} & \frac{\partial G_u(\mathbf{A}, p_i, q_i)}{\partial y} & \frac{\partial G_u(\mathbf{A}, p_i, q_i)}{\partial z} & \frac{\partial G_u(\mathbf{A}, p_i, q_i)}{\partial u} & \frac{\partial G_u(\mathbf{A}, p_i, q_i)}{\partial v} \\ \frac{\partial G_v(\mathbf{A}, p_i, q_i)}{\partial x} & \frac{\partial G_v(\mathbf{A}, p_i, q_i)}{\partial y} & \frac{\partial G_v(\mathbf{A}, p_i, q_i)}{\partial z} & \frac{\partial G_v(\mathbf{A}, p_i, q_i)}{\partial u} & \frac{\partial G_v(\mathbf{A}, p_i, q_i)}{\partial v} \end{bmatrix}$$

In addition, $\mathbf{J}_{\mathbf{A}}$ denotes the Jacobian of the function G with respect to the twelve parameters of the transformation matrix \mathbf{A} , which map the parameter vector A_i to the output

$$A_{12} \cdot \mathbf{J}_{\mathbf{A}} = \left[\mathbf{J}_{A_1} \cdots \mathbf{J}_{A_n} \right]^T,$$

$$\mathbf{J}_{A_i} = \begin{bmatrix} \frac{\partial G_u(\mathbf{A}, p_i, q_i)}{\partial A_1} & \dots & \frac{\partial G_u(\mathbf{A}, p_i, q_i)}{\partial A_{12}} \\ \frac{\partial G_v(\mathbf{A}, p_i, q_i)}{\partial A_1} & \dots & \frac{\partial G_v(\mathbf{A}, p_i, q_i)}{\partial A_{12}} \end{bmatrix}$$

We can obtain $\Sigma_{\mathbf{A}} = (\mathbf{J}_{\mathbf{A}}^{-1}) \cdot (\mathbf{J}_{\mathbf{a}} \Sigma_{\mathbf{a}} \mathbf{J}_{\mathbf{a}}^T) \cdot (\mathbf{J}_{\mathbf{A}}^{-1})^T$.

For the computation of the three-dimensional target point coordinates, considering Eq. (5), we denote $H(\mathbf{q}_{\text{aim}}, \boldsymbol{\beta}) = 0$ as the mapping function, where $\boldsymbol{\beta} = [\mathbf{p}_1^T, \mathbf{p}_2^T, \mathbf{A}^T, \mathbf{B}^T]^T$ represents the associated input variables. Let $\Sigma_{\mathbf{q}_{\text{aim}}}$ denote the covariance matrix of the output vector $H(\mathbf{q}_{\text{aim}}, \boldsymbol{\beta}) = 0$ of $H(\mathbf{q}_{\text{aim}}, \boldsymbol{\beta}) = 0$, and let $\Sigma_{\boldsymbol{\beta}}$ denote the covariance matrix of the output vector $\boldsymbol{\beta}$. According to the uncertainty propagation principle, the resulting covariance is given by

$$\mathbf{J}_{\mathbf{q}_{\text{aim}}} \Sigma_{\mathbf{q}_{\text{aim}}} \mathbf{J}_{\mathbf{q}_{\text{aim}}^T} = \mathbf{J}_{\boldsymbol{\beta}} \Sigma_{\boldsymbol{\beta}} \mathbf{J}_{\boldsymbol{\beta}}^T.$$

Where

$$\mathbf{J}_{\mathbf{q}_{\text{aim}}} = \begin{bmatrix} \frac{\partial G_x(\mathbf{A}, p_1, q_1)}{\partial x} & \frac{\partial G_x(\mathbf{A}, p_1, q_1)}{\partial y} & \frac{\partial G_x(\mathbf{A}, p_1, q_1)}{\partial z} \\ \frac{\partial G_y(\mathbf{B}, p_2, q_2)}{\partial x} & \frac{\partial G_y(\mathbf{B}, p_2, q_2)}{\partial y} & \frac{\partial G_y(\mathbf{B}, p_2, q_2)}{\partial z} \end{bmatrix}$$

$$, \quad \Sigma_{\boldsymbol{\beta}} = \text{diag}\{\Sigma_{p_1}, \Sigma_{p_2}, \Sigma_{\mathbf{A}}, \Sigma_{\mathbf{B}}\},$$

$$\mathbf{J}_{\boldsymbol{\beta}} = \begin{bmatrix} \mathbf{J}_{p_1} & \mathbf{0} & \mathbf{J}_{\mathbf{A}} & \mathbf{0} \\ \mathbf{0} & \mathbf{J}_{p_2} & \mathbf{0} & \mathbf{J}_{\mathbf{B}} \end{bmatrix},$$

$$\mathbf{J}_{p_1} = \begin{bmatrix} \frac{\partial G_x(\mathbf{A}, p_1, \mathbf{q}_{\text{aim}})}{\partial u} & \frac{\partial G_x(\mathbf{A}, p_1, \mathbf{q}_{\text{aim}})}{\partial v} \\ \frac{\partial G_y(\mathbf{A}, p_1, \mathbf{q}_{\text{aim}})}{\partial u} & \frac{\partial G_y(\mathbf{A}, p_1, \mathbf{q}_{\text{aim}})}{\partial v} \end{bmatrix},$$

$$\mathbf{J}_{p_2} = \begin{bmatrix} \frac{\partial G_x(\mathbf{B}, p_2, \mathbf{q}_{\text{aim}})}{\partial u} & \frac{\partial G_x(\mathbf{B}, p_2, \mathbf{q}_{\text{aim}})}{\partial v} \\ \frac{\partial G_y(\mathbf{B}, p_2, \mathbf{q}_{\text{aim}})}{\partial u} & \frac{\partial G_y(\mathbf{B}, p_2, \mathbf{q}_{\text{aim}})}{\partial v} \end{bmatrix},$$

$$\mathbf{J}_{\mathbf{A}} = \begin{bmatrix} \frac{\partial G_x(\mathbf{A}, p_1, \mathbf{q}_{\text{aim}})}{\partial A_1} & \dots & \frac{\partial G_x(\mathbf{A}, p_1, \mathbf{q}_{\text{aim}})}{\partial A_{12}} \\ \frac{\partial G_y(\mathbf{A}, p_1, \mathbf{q}_{\text{aim}})}{\partial A_1} & \dots & \frac{\partial G_y(\mathbf{A}, p_1, \mathbf{q}_{\text{aim}})}{\partial A_{12}} \end{bmatrix},$$

$$\mathbf{J}_{\mathbf{B}} = \begin{bmatrix} \frac{\partial G_x(\mathbf{B}, p_2, \mathbf{q}_{\text{aim}})}{\partial B_1} & \dots & \frac{\partial G_x(\mathbf{B}, p_2, \mathbf{q}_{\text{aim}})}{\partial B_{12}} \\ \frac{\partial G_y(\mathbf{B}, p_2, \mathbf{q}_{\text{aim}})}{\partial B_1} & \dots & \frac{\partial G_y(\mathbf{B}, p_2, \mathbf{q}_{\text{aim}})}{\partial B_{12}} \end{bmatrix}$$

The pseudoinverse can thus be obtained as

$$\Sigma_{\mathbf{q}_{\text{aim}}} = \mathbf{J}_{\mathbf{q}_{\text{aim}}}^{-1} \mathbf{J}_{\boldsymbol{\beta}} \Sigma_{\boldsymbol{\beta}} \mathbf{J}_{\boldsymbol{\beta}}^T (\mathbf{J}_{\mathbf{q}_{\text{aim}}}^T)^{-1} \quad (16)$$

II. EXPERIMENTS AND ANALYSIS

A. Simulation Setup

3.2.1 Biplanar X-ray Imaging and Reconstruction

In simulation, biplanar X-ray imaging is modeled using a pinhole camera formulation. For each control point,

$$\lambda x_i = P \tilde{X}_i, \quad (17)$$

where x_i denotes homogeneous pixel coordinates, P is the projection matrix, and \tilde{X}_i represents the potentially perturbed 3D control point. Projection matrices are estimated using DLT and least squares from multiple 3D–2D correspondences, and the target point is reconstructed via biplanar triangulation to obtain \hat{X} .

3.2.2 Error Source Modeling

Two primary error sources are considered. Pixel detection noise is modeled as zero-mean Gaussian noise added to 2D observations. Installation error is treated as a structural perturbation, where the 3D control point input is perturbed by small rotations and translations:

$$\tilde{X}_i = T(\delta\theta, \delta t) X_i. \quad (18)$$

To reflect the execution chain in robotic navigation, the transformation from the reconstructed target to the robot TCP frame is included, with an additional installation error introduced between the mounting component and the end effector.

3.2.3 Evaluation Metrics

Performance is evaluated using the 3D localization error, TCP execution error, and average reprojection error. Tail-risk behavior is characterized using the 95th percentile (P95) and worst-case error to capture extreme failure modes arising from nonlinear geometric estimation.

B. Simulation III: Analytic Uncertainty Propagation versus Monte Carlo

The third simulation evaluates the predictive capability of the proposed error propagation model. Under a representative operating condition, output error covariances are computed using both Monte Carlo sampling and first-order uncertainty propagation.

The comparison shows that analytic propagation accurately predicts dominant error directions and relative magnitudes, while underestimating absolute variance under strongly nonlinear conditions. This suggests that the analytic model is effective for sensitivity analysis, whereas statistical methods are required for reliable tail-risk assessment.

III. SIMULATION RESULTS

To systematically validate the proposed system-level error propagation mechanism in biplanar X-ray-guided navigation, three simulation studies are conducted to analyze:

- (1) the primary effect of installation error
- (2) the coupled amplification between installation error and pixel noise, and
- (3) the predictive capability of first-order analytic uncertainty propagation.

All simulations are based on the biplanar pinhole imaging model described in Section III and evaluated using Monte Carlo

sampling with 2000 trials per configuration. Both 3D localization error and TCP execution error are reported, together with tail-risk metrics to characterize worst-case behavior.

A. Simulation Study I: Primary Effect of Installation Error

We first analyze the direct impact of reference structure installation error on localization and execution accuracy. Rotational and translational installation errors are independently scanned while pixel noise is fixed at a low level, so as to isolate the dominant effect of installation-induced structural perturbations.

1) Rotational Installation Error

Quantitative results are summarized in Table S1. Increasing the rotation misalignment from 0° to 2° amplifies the mean localization error from approximately 18 mm to over 75 mm. Meanwhile, the P95 tail risk of the TCP execution error nearly doubles, rising from about 45 mm to close to 90 mm.

It is important to note that, in this experiment, the TCP transformation is assumed to be an ideal rigid-body mapping without additional execution uncertainty. Consequently, the execution error magnitude matches the localization error magnitude. This observation does not imply that the execution chain is insensitive to error, but rather indicates that structural installation error introduced at the perception and reconstruction stages alone is sufficient to determine the upper bound and tail-risk behavior of navigation accuracy.

Table S1. Effect of installation rotation and translation errors on localization accuracy (Sim1)

Installation Error	e_{3D} (mm)	e_{TCP} (mm)	P95 e_{TCP} (mm)
Rotation 0.0°	0.018	0.018	0.045
Rotation 0.5°	0.027	0.027	0.048
Rotation 1.0°	0.042	0.042	0.058
Rotation 1.5°	0.058	0.058	0.070
Rotation 2.0°	0.075	0.075	0.086
Translation 0 mm	0.019	0.019	–
Translation 1 mm	0.018	0.018	–
Translation 2 mm	0.019	0.019	–
Translation 3 mm	0.018	0.018	–
Translation 4 mm	0.019	0.019	–
Translation 5 mm	0.019	0.019	–

2) Translational Installation Error

As reported in Table S1, translational misalignment within the range of 0–5 mm results in only marginal variations in both localization and execution error, with error magnitudes remaining nearly constant.

B. Simulation Study II: Coupled Amplification of Installation Error and Pixel Noise

In practical systems, installation error and pixel-level perception noise coexist. To investigate their interaction, we perform a coupled simulation study by jointly varying installation error levels (L0–L2) and pixel noise magnitude.

This behavior is quantitatively summarized in Table S2. For example, under moderate pixel noise, the P95 TCP error increases from 90.39 mm at L0 to 108.56 mm at L2. Under high pixel noise, tail risk exceeds 200 mm regardless of whether installation error is present, indicating that the system has entered a high-risk regime.

These results demonstrate that system error is not a simple additive combination of perception noise and installation error. Instead, installation error fundamentally alters the system's sensitivity to pixel-level uncertainty, transforming otherwise tolerable noise into a navigation-level risk factor through structural coupling in the geometric estimation pipeline.

Table S2. Coupled amplification of pixel noise and installation error (P95 of execution error)

Installation Level	$\sigma_{px} = 0 \text{ px}$	$\sigma_{px} = 2 \text{ px}$	$\sigma_{px} = 5 \text{ px}$
L0 (0° + 0 mm)	0.00 mm	0.090 mm	0.240 mm
L1 (1° + 2 mm)	0.036 mm	0.098 mm	0.242 mm
L2 (2° + 5 mm)	0.072 mm	0.108 mm	0.219 mm

C. Simulation Study III: Analytic Uncertainty Propagation versus Monte Carlo Statistics

To further evaluate the predictive capability of the proposed error propagation model, we compare first-order analytic uncertainty propagation with Monte Carlo statistics under a representative operating condition.

Table S3 provides a quantitative comparison between analytic and Monte Carlo results. While the analytic model predicts the correct ordering and anisotropy of error components, the depth-direction standard deviation is underestimated by approximately a factor of two. This behavior is consistent with the linearization assumptions underlying first-order propagation and highlights its inherent limitations under strong nonlinear geometric conditions.

Rather than constituting a deficiency, this comparison clarifies the complementary roles of analytic and statistical approaches: analytic propagation provides interpretable sensitivity analysis and directional insight, while Monte Carlo sampling is necessary for reliable tail-risk estimation in nonlinear regimes.

Table S3. Comparison of analytic and Monte Carlo uncertainty propagation (Sim3)

Axis	MC Mean (mm)	ANA Mean (mm)	MC Std (mm)	ANA Std (mm)
X	0.602	0.602	0.015	0.010
Y	0.515	0.515	0.010	0.008
Z	0.221	0.220	0.043	0.019

Across the three simulation studies, the results consistently indicate that installation error acts as a primary driver of system-level error propagation in biplanar X-ray navigation. Rotational misalignment governs localization accuracy and tail-risk behavior, installation error and pixel noise exhibit coupled amplification, and first-order analytic propagation captures dominant sensitivity structure while requiring statistical evaluation for worst-case risk assessment.

IV. REAL-SYSTEM VALIDATION

Table S4 summarizes the localization error statistics under different installation error levels. Regardless of whether 3D localization error or reprojection error is used, the error magnitude exhibits a clear monotonic increase across installation levels, i.e., L0 < L1 < L2. Under ideal installation conditions (L0), the localization error remains at a relatively low level of 0. Introducing moderate installation error (L1) increases the mean error to 0.551, while larger misalignment (L2) further degrades accuracy to 1.380. These results indicate that installation perturbations significantly deteriorate localization accuracy in a real biplanar navigation pipeline.

Beyond mean error, tail-risk metrics show an even more pronounced dependence on installation error. As the installation level increases, the growth of P95 substantially exceeds that of the mean error, indicating that installation error not only elevates overall error magnitude but also markedly amplifies worst-case behavior. This observation is consistent with the simulation results, which identified structural installation error as the dominant contributor to tail-risk amplification.

For quantitative comparison, Table S4 reports the mean error, standard deviation, and P95 values under each installation level. As shown in the table, both 3D localization error and reprojection error increase consistently with installation misalignment, with P95 being particularly sensitive to changes in installation state. This further confirms that installation error is systematically amplified through the geometric reconstruction chain in real systems.

Table S4. Real-system validation results under different installation error levels

Level	Nominal misalignment	Mean e_{3D} (mm)	Std e_{3D} (mm)	P95 e_{3D} (mm)	Mean e_{reprj} (px)
L0	0.000	0.000	0.000	0.000	0.000
L1	~1° / 2 mm	0.551	0.0046	0.556	2.0
L2	~2° / 5 mm	1.380	0.0110	1.391	5.0